ARTICLE   OPEN

Check for updates

TEM and EELS characterization of Ni–Fe layered double hydroxide decompositions caused by electron beam irradiation

Christopher Hobbs[1,2], Clive Downing[2,3], Sonia Jaskaniec [ID][2,4] and Valeria Nicolosi [ID][2,3,4 ✉]

Electron irradiation of Ni–Fe layered double hydroxides (LDHs) was investigated in the transmission electron microscope (TEM). The initial structure possessed a flat hexagonal morphology made up of crystalline domains with a well-defined hexagonal crystal structure. The Ni–Fe LDHs were susceptible to significant structural decompositions during electron irradiation. The generation of pores and crystallographic breakdown of the LDH routinely occurred. In addition, a compositional change was established by electron energy loss spectroscopy (EELS). During 300 kV irradiation, a pre-peak evolution in the oxygen K edge highlighted a transition to metal oxide species. In parallel, nitrogen K edge attenuation demonstrated interlayer mass-losses. It was found that TEM conditions profoundly affected the decomposition behaviours. At lower acceleration voltages, an increased dehydration rate of the LDH cationic layers is observed during irradiaton. Moreover, in situ specimen cooling revealed the retention of interlayer nitrates. An emphasis on the dehydroxylation processes and anionic mass-loss facilitation is discussed.

INTRODUCTION

The scientific interest in transition metal-based layered double hydroxides (LDH) has led to an exhibition of applications across nanotechnology in areas such as batteries, water splitting and nanomedicine[1–6]. In particular, the latest studies involving nickel and iron LDHs have placed these materials at the frontier of oxygen evolution reaction research[7,8]. Such versatility is largely owed to their inherent physical and chemical features including surface areas, controllable synthesis methods, compositional tunability and favourable interactions to form composites[9,10]. Recently, researchers have progressed the development and application of various LDH materials down to the atomic scale[11,12]. This is also partnered with a fascination of how these materials attain their associated structures and properties. This combination indeed justifies a necessity to provide a full understanding of these materials from all aspects of nanotechnology[13,14]. In this regard, transmission electron microscopy (TEM)/scanning TEM (STEM) can reveal a wide range of physical phenomena at high spatial and energy resolutions. Simultaneously, a further wealth of knowledge can be provided using complementary techniques such as electron energy loss spectroscopy (EELS). This entails the probing of core and valence level excitations caused by the incident beam, where electrons are collected based on their energy after interacting with the specimen. Thus revealing electronic structure and bonding information at very high spatial resolutions down to single-atom levels[15]. A schematic of the TEM and EELS imaging principles along with a crystallographic representation of a typical LDH structure is displayed in Fig. 1. However, an established drawback of TEM is electron beam-induced sample damage caused by complex interaction mechanisms such as radiolysis, atomic displacement (so-called 'knock-on') and Joule heating[16–18]. The electron beam has the ability to structurally and chemically change these types of materials during TEM characterization. These limitations are of distinct prominence in the study of electron beam-sensitive materials, such as metallic hydroxides and oxides[19–21]. The Ni–Fe LDH falls under this

category, having previously been established as being susceptible to beam damage[22]. As such, the TEM characterization of Ni–Fe LDH materials requires particular attention to achieve correct structure-property relationships and establish a thorough understanding of the observed features in the electron microscope. To date, an in-depth study of potential Ni–Fe LDH decompositions by electron irradiation is yet to be explored. Fortunately, the inherent properties of these material types are suitable for such TEM analysis. These include highly crystalline properties yielding well-defined electron diffraction features, suitably placed EELS ionization edges on the energy loss spectrum, thin 'electron transparent' morphologies and uniform dispersions allowing characterization at very high spatial resolutions on the single-particle level. In this report, we utilised TEM and core loss EELS to investigate the extent of electron beam-induced transformations of Ni–Fe LDHs physical and chemical properties. We also further examine how the TEM imaging conditions can affect the observed transformations as a consequence by the electron beam irradiation effects.

RESULTS AND DISCUSSION

Electron irradiation of Ni–Fe LDHs at 300 kV

Our synthesis methods provide large quantities of high-quality Ni–Fe LDH samples with suitable dispersions for TEM analysis on the single-particle level[23,24]. The properties of the Ni–Fe LDH materials were extensively characterized using 'bulk' techniques such as XRD and FTIR throughout these works. From a TEM perspective, the well-defined morphology and crystal symmetry offer a suitable framework for our following studies. The 'two-dimensional' nature of the nanoplatelets allowed for suitable EELS counts above background levels to be extracted and studied. Along with this, the oxygen, nickel and iron ionization edges are well defined and suitably placed on the core loss energy loss spectrum for simultaneous analysis during irradiation experiments[25–27]. As a first reference, the structural features of the Ni–Fe LDH nanomaterial were initially characterized using TEM, selected

¹School of Physics, Trinity College Dublin, Dublin, Ireland. ²CRANN & AMBER, Trinity College Dublin, Dublin, Ireland. ³The Advanced Microscopy Laboratory, Trinity College Dublin, Dublin, Ireland. ⁴School of Chemistry, Trinity College Dublin, Dublin, Ireland. ✉email: nicolov@tcd.ie
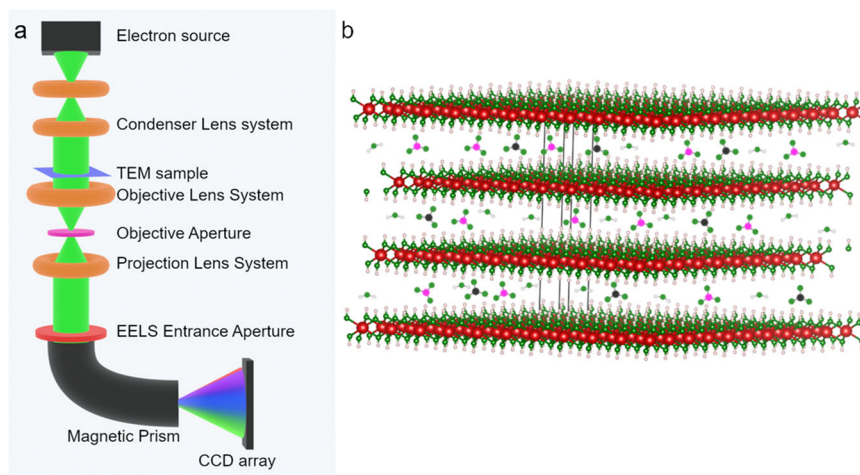
npj nature partner journals

Fig. 1   TEM imaging principles and LDH structure. a Schematic of TEM and EELS methodologies. **b** Crystallographic depiction of the Ni–Fe LDH nanomaterial. Atomic elements are portrayed as nickel/iron (red), oxygen (green), hydrogen (white), carbon (black), nitrogen (pink). Components of schematic not to scale.
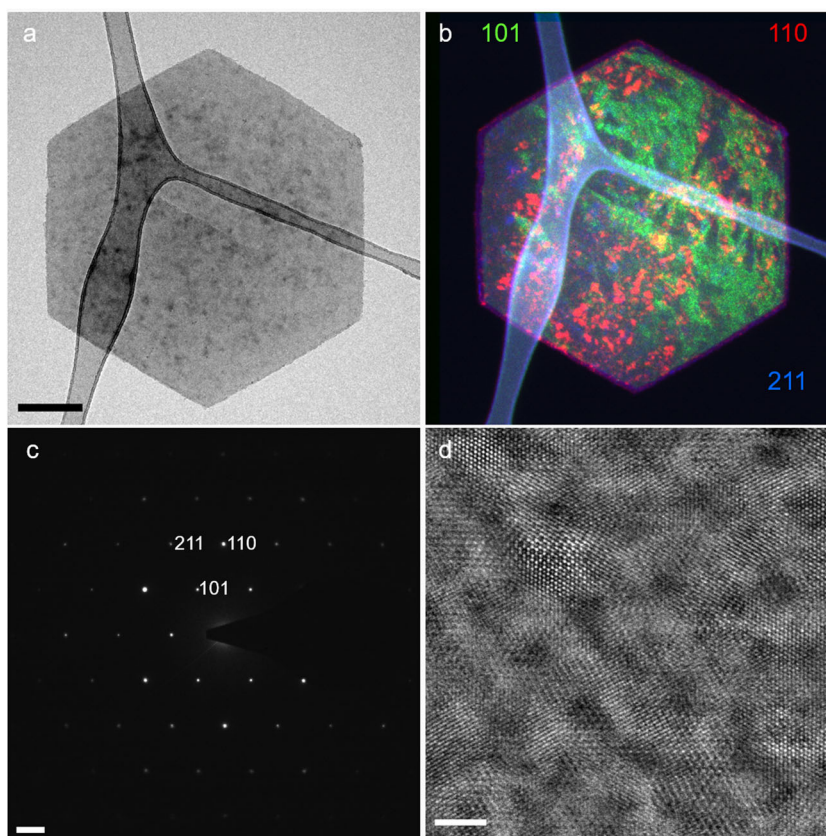

Fig. 2   TEM characterization of Ni–Fe LDH material. a Bright-field TEM image of a representative Ni–Fe LDH nanoplatelet. **b** Composite dark-field TEM images acquired from the (101), (110) and (211) reciprocal lattice vectors in green, red and blue respectively. **c** Typical electron diffraction pattern of the Ni–Fe LDH. The {101} and {110} planar families are annotated on the diffraction pattern. **d** Aberration-corrected STEM micrograph of the Ni–Fe LDH material. Scale bars are 200 nm, 2 nm^{-1} and 2 nm for the **a** BFTEM image, **c** SAED pattern and **d** HAADF-STEM micrograph respectively.

area electron diffraction (SAED) and HAADF-STEM methods (Fig. 2). The Ni–Fe LDH material was found to attain a hexagonal morphology with a lateral dimension of ~700 nm[24]. The LDH SAED patterns exhibit highly crystalline hexagonal symmetries (Fig. 2(c)), with interplanar spacings of 7.4 nm^{-1} and 12.9 nm^{-1} corresponding to the LDH {100} and {110} families respectively. The varying contrasts of the dark-field TEM experiments

showcased that the morphology of the LDH is composed of small arrangements of randomly oriented crystallites within the LDH platelet (Fig. 2b). This is highlighted by the colour composite dark-field TEM image from the 101 (green), 110 (red) and 211 (blue) reciprocal lattice vectors. This indicates that the LDH platelet is composed of a crystallite assembly lying on various crystal-lographic axes. Moreover, this is directly observed in our

HAADF-STEM studies where the varying degrees of orientations is evidenced from the crystallites lying on different axes throughout the material (Fig. 2d). After establishing the initial physical features of the Ni–Fe LDH, the sample was subjected to electron irradiation in the TEM. The electron beam continuously illuminated the region of interest and TEM images were acquired at sporadic time intervals. Electron diffraction patterns were also recorded before and after irradiation to investigate the change in crystal structure caused by the beam. Corresponding time series EELS spectra were recorded during irradiation of a new sample area. A 0.1 eV/channel for the EELS spectrometer was used to capture the nitrogen K and oxygen K core loss edges. This was followed by a similar time-series study of the metallic nickel $L_{2,3}$ and Fe $L_{2,3}$ ionization edges. In this case, a 0.2 eV/channel was utilized to record the full edge profiles associated with the nickel, iron and oxygen sites of the LDH sample. Spectra were acquired using <1 s exposures and summing between 10–15 frames. The electron dose rates used were 4.46×10^7 e nm^{-2} s^{-1} and 1.82×10^7 e nm^{-2} s^{-1} for TEM and EELS experiments respectively. These dose rates were kept consistent in subsequent studies, within the limits of TEM instrumentation capabilities. Additional experimental details can be found in the 'Methods' section. The effect of electron irradiation on the NiFe LDH is displayed in Fig. 3. Bright-field TEM was used to capture the morphology of the LDH material (Fig. 3b–e). The time denoted on each image represents the time after initial image acquisition. The LDH material is observed to develop from a uniform lamellar material into a structure containing crystallites and voids after the sample was irradiated with the electron beam for 728 s. This decomposition behaviour is comparable to previous studies involving similar structures[21,28]. Although the overall hexagonal shape of the Ni–Fe LDH nanoplatelet remains, there is a notable development of a porous morphology, as depicted in Fig. 3 (b–e). Interestingly, the edges of the material do not appear to generate pores, perhaps due to the different local chemistry in these regions compared to the centre sites. An inspection of the corresponding electron diffraction patterns highlights a crystallographic breakdown of the material, evidenced by the intensity attenuation of the {100} planes as well as the full width half maximum (FWHM) broadening of the {110} diffraction spots from 0.42 nm^{-1} to 1.02 nm^{-1} after 728 s (Fig. 3a, f). The corresponding d-spacing of the {100} and {110} planes also decreased from 2.71 nm to 2.51 nm and 1.58 nm to 1.51 nm respectively. This indicates a dehydration of the material, although this interpretation can be difficult to discern from in-plane layer spacing changes[20,29]. The chemical and electronic structure of the Ni–Fe LDH was investigated using EELS, as shown in Fig. 3g. The specified time on each spectrum represents the accumulated exposure time after initial acquisition. Initially, the oxygen K ionization edge occurs at 546 eV (peak iii, Fig. 3g). This is a result of O 1s to O 2p state core level excitations from the oxygen sites octahedrally coordinated to the iron and nickel cations, as well as interstitial species such as water and CO_3^{3-} and NO^{3-}. Similarly, the delayed onset nitrogen K edge is exhibited at 406 eV. This is attributed to nitrates adhered to the surface and anionic species in the inter-gallery regions of the LDH. As the sample is electron-irradiated, there are two distinct changes observed in the time series EELS time series. (Fig. 3g). Firstly, the nitrogen K edge disappears under electron irradiation (peak i, Fig. 3g). The intensity of this spectral peak, relative to the main oxygen K edge intensity, decreases from 0.17 to 0 after 1174 s of irradiation. This induced damage is likely due to the escape of nitrogen from the interlayer galleries through the generated pores, basal planes, crystal breakdown or restructure. Secondly, there is the appearance of a peak in the O K ELNES at 538 eV (peak ii, Fig. 3g). This pre-peak of the O K edge is attributed to the O 1s excitation to a hybridized state of the O 2p band with 3d band of the associated Ni or Fe transition metals in the LDH cationic layers. We propose that this is due to the creation of transition metal oxides (TMO) within the

porous structure induced by the electron beam interaction[30,31]. One potential beam-induced mechanism causing this reconstruction is the removal of hydrogen from the hydroxyl groups of the LDH layers, caused by scission of the O–H bonds or 'knock-on' of the hydrogen sites within the OH groups of the primary LDH structures. This is followed by the structural reconstruction of a TMO species. Interestingly, this behaviour appears to be dependent on the nature of the LDH metallic sites. Our comparative studies of Mg-Al LDH composition did not show the evolution of a pre-peak in the ELNES of the oxygen K edge, negating previously reported data stating that this peak could potentially be due to the presence of O–O bonds caused during irradiation (see Supplementary Information)[32,33]. The electronic structure of the transition metals in the cationic layers was also probed on a fresh sample area using a time-resolved EELS approach. Figure 4 shows the associated EELS spectra of the nickel and iron $L_{2,3}$ edges of the Ni-Fe LDH material. The oxygen K edge was also recorded for comparative purposes. In this instance, a 0.2 eV/channel spectrometer dispersion was used, and the specimen was subjected to a dose rate of 2.8×10^7 e nm^{-2} s^{-1}. Figure 4 portrays the effect of electron irradiation on the Ni and Fe $L_{2,3}$ ionization edges. In this experimental set-up, the initial EELS spectrum shows the oxygen K edge at 546 eV, as previously seen in Fig. 3g. Peaks iv and v at 714.5 eV and 728.2 eV correspond to the iron L_3 and L_2 edges (Fig. 4). Analogously, peaks vi and vii at 859.1 eV and 876.7 eV derive from the nickel L_3 and L_2 edges respectively (Fig. 4)[25]. The EELS features are due to excitations from 2p states to localized 3d states with a degeneracy of the 2p states into the $2p_{1/2}$ (L_2) and $2p_{3/2}$ (L_3) from the spin-orbit coupling of the metallic sites in the cationic LDH layers. During irradiation of 1154 s, these L edges do not experience any significant change during irradiation. The L_3 to L_2 peak separation remained relatively constant throughout at 13.1 eV and 17.5 eV for the respective Fe and Ni sites. Similarly, the respective white line intensity ratios remain unchanged from 0 s to 1154 s, evaluated as 5.43 and 3.47. The shape of the Fe and Ni edges did not undergo any alterations during this time frame. This advocates no major comprehension of the valency or oxidation states of the transition metals after the electron beam interactions[34]. In contrast, the oxygen ELNES pre-edge profile changes as previously observed (Fig. 3g), with the formation of the pre-peak in the oxygen K edge at 534 eV after 1154 s. This is also accompanied with an additional peak in the O K edge at 579.5 eV after 379 s of beam exposure. Both of these features remained until after the total exposure time of 1154 s and can be assigned to the formation of Ni–O structures[25,35,36]. An equivocal case may also be made for the generation of Fe–O species derived during irradiation as a result of radiolysis of oxygen bonds (H_2O, O and OH) within the LDH layers or galleries[26,37]. Up until now, our experimental set-up infers a multitude of possible mechanisms causing the observed decompositions of electron-irradiated Ni–Fe LDHs such radiolysis, atomic 'knock-on' and localized heating. We next investigate how varying the TEM experimental conditions could mitigate some of these processes, namely cooling the specimen and reducing the incident acceleration voltage.

Irradiation of Ni–Fe LDHs at cryogenic temperatures

By cooling the specimen in the TEM, we hope to reduce the effect of Joule heating, thermal diffusion and adatom vibrations, all of which may contribute to the already observed decompositions of the Ni–Fe LDH. These potential influences were investigated by conducting parallel EELS experiments, where the sample was analysed at $-180\,°C$. A fresh LDH sample was analysed using TEM methods during continuous beam exposure at a dose rate of 1.72×10^7 e nm^{-2} s^{-1}. Subsequent EELS spectra were also acquired, summing over 10 frames of 0.5 s each. Figure 5 displays the SAED (a) and (f), BFTEM (b)–(e) and core loss EELS (g) analysis
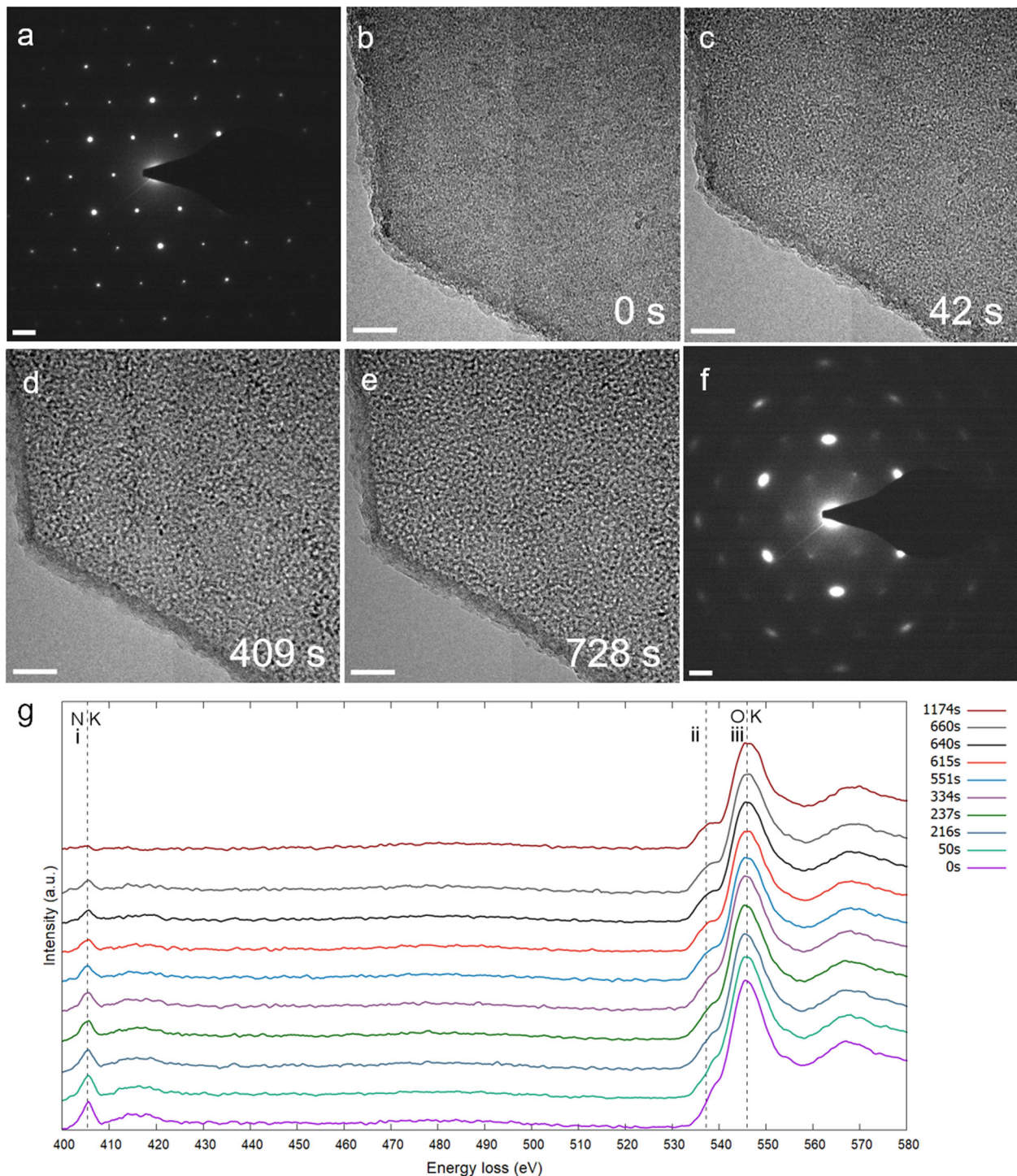
Fig. 3 Electron irradiation of Ni–Fe LDH at 300 kV. a, f SAED pattern recorded before and after irradiation by electron beam. **b–e** Time series TEM micrographs acquired of the same Ni–Fe LDH region. Images acquired after 0 s, 42 s, 409 s and 728 s of beam exposure respectively. **g** EELS spectra time series of the nitrogen K edge and oxygen K edge from 0 s to 1174 s. The time associated with each spectra represents the amount of irradiation time by the electron beam at acquisition. Scale bars are $2\,nm^{-1}$ for the SAED patterns and 20 nm for the BFTEM micrographs respectively.

of the Ni–Fe LDH during 300 kV electron irradiation as the sample is cooled to −180 °C in situ. In a similar fashion to room temperature TEM experiments (Fig. 3), the LDH platelets develop a porous morphology during this irradiation. This is exhibited after 120 s (Fig. 5d) with an overall increase in pore size as this continues to 375 s (Fig. 5e). A crystal structure breakdown of the LDH is also apparent, whereby the FWHM of the {110} planes

increases from $0.17\,nm^{-1}$ to $0.71\,nm^{-1}$ (Fig. 5a, f). Along with this, the {100} d-spacings reduced from 2.71 nm to 1.88 nm. This is a more pronounced change from the room temperature counterpart irradiation experiments. Although in either case, the reductions suggest that they are not induced by electron beam heating. In this instance, the parallel core loss EELS highlighted an increased dehydration rate (Fig. 5g). After 195 s of irradiation, a
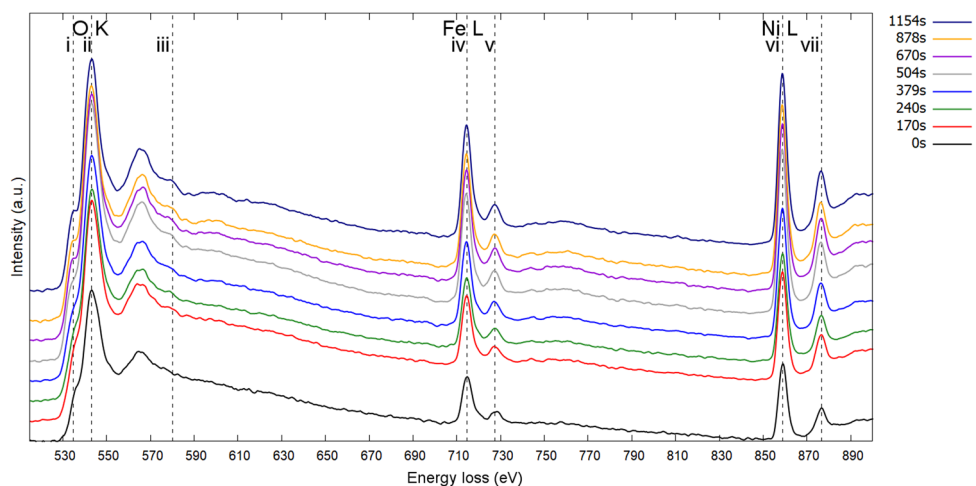
Fig. 4 Time series core loss EEL spectra of the oxygen K edge, iron L2,3 edge and nickel L2,3 ionization edges acquired at 300 kV. Each spectra is associated with the amount of time it is exposed to the electron beam.

peak at 534.0 eV develops, with an intensity ratio increase from 0 to 0.06. This is compared to the ambient temperature experiments where similar intensity levels of this pre-edge feature occurred at 1174 secs (Fig. 3 g). This induced H removal and in-plane crystal degradations appear to be independent of the sample's thermal conditions, suggesting that it is created from a knock-on or radiolytic interaction as opposed to a heating effect. A further attribution is the potential sputtering effects caused by small amounts of adhered contamination, such as water-based radicals, within the TEM column onto the sample. This may accelerate the removal of hydrogen from LDH hydroxyl groups causing greater effects of in-plane crystal degradations. Furthermore, the cooling revealed that the nitrogen peak intensity is preserved during irradiation (peak i, Fig. 5g). The intensity ratio of the nitrogen K edge at 403.5 eV remains constant at ~0.23 (relative to the O K edge) from the initial spectrum acquisition to 475 s. This feature was retained even after 1255 s (see Supplementary Information). We accredit this to the preservation of NO_3^- groups within the LDH materials during electron beam exposures as a consequence of cooling the specimen to cryogenic temperatures. The behaviour of the Ni $L_{2,3}$ and Fe $L_{2,3}$ edges were also used to investigate the electronic structure of the metallic sites of the LDH material. Our time series EELS of the transition metal L edges showed that the white line intensity ratio remained unchanged at 5.88 from 0 s to 819 s of irradiation. Comparing to room temperature experiments, no major change in oxidation states of the Ni or Fe $L_{2,3}$ edges was observed. However, enhanced EELS energy resolution or greater dose rates may have presented more pronounced oxidation effects from these transition metals[19]. In parallel analysis of the oxygen K edge at 534 eV it is also observed that there was no peak formation at 579.5 eV up to 819 s, suggesting that this post-edge peak generation is due to thermal effects. (see Supplementary Information)[38].

Irradiation of Ni–Fe LDH at 80 kV

We subsequently orchestrated parallel 80 kV TEM and EELS experiments to investigate the role of the incident electron energy on the observed transformations. At this acceleration voltage, the sample becomes more susceptible to inelastic interactions and increased radiolysis but knock-on damage can be subsided if the incident energy is less than the displacement energy of each atom in the structure[17]. Figure 6 displays comparable 80 kV experiments to the previously conducted analyses at 300 kV. In this case, the Ni–Fe LDHs were subjected to an electron dose rate of 2.31×10^7 e nm^{-2} s^{-1} and 2.10×10^7 e nm^{-2} s^{-1} for TEM

and EELS studies respectively. As is the case with the 300 kV experimentations, the generation of a voided morphology is once again observed (Fig. 6b–e). It is argued that this degradation occurs more abruptly, as the fully formed pores can be seen after 141 s of irradiation (Fig. 6d). This is corroborated by a crystallographic breakdown after 205 s (Fig. 6f), depicted by an intensity attenuation of the {100} and long-range order diffraction spots, as well as a FWHM increase of the {110} spots from 0.31 nm^{-1} to 0.94 nm^{-1} [39]. This is further substantiated by EELS analysis of the N K and O K edges conducted during irradiation at 80 kV (Fig. 6g). Coincidentally, the disappearance of the nitrogen K-edge at 406 eV (peak i, Fig. 6g) is accelerated at 80 kV. The intensity of the nitrogen K edge, relative to the main O K edge at 546 eV (peak iii, Fig. 6g), decreases from 0.31 to 0.02 after 141 s. The decomposition of the cationic sites and nitrogen-based mass losses of the LDH structure occurs more rapidly at 80 kV. This is portrayed from the generation of the transition-metal oxide EELS signatures after only 88 s (peak ii, Fig. 6g) of irradiation in comparison to 1174 s at 300 kV (Fig. 3g). At 80 kV, the pre-peak of the oxygen K edge increases from 0.04 to 0.16 after 141 s of irradiation. This contrasts the pre-peak intensity ratio increase from 0 to 0.09 during 475 s of irradiation conducted at 300 kV at cryogenic temperatures (Fig. 5g). We infer that this is because of a further dehydration of the Ni–Fe LDH at 80 kV. There is also a more distinct peak shape in contrast to the shoulder generated by the 300 kV experiments at room and cryogenic temperatures (Fig. 3g and Fig. 5g respectively). Moreover, the generation of this O K edge feature occurred at a noticeably faster rate relative to the previous 300 kV experiments. The oxygen core loss EELS feature changes occurred at 80 kV after 102 s in comparison to the 300 kV where they occurred at 1174 s of electron irradiation. It's speculated that this is due to the increased inelastic interactions at the lower incident voltage, prompting greater effects of radiolysis and thermally related damage to the LDH specimens. We subsequently carried out EELS experiments of the nitrogen and oxygen core loss K edges to examine the role of thermally induced transformations whilst the sample was irradiated at 80 kV and cooled in situ to liquid nitrogen temperatures. Figure 7 displays the time series EELS studies of the Ni–Fe LDH at 80 kV when the sample is cooled to −180 °C. In this instance, the Ni–Fe LDH was subjected to a dose rate of 0.66×10^7 e nm^{-2} s^{-1}. Notably, the nitrogen K edge, at ~403.5 eV (peak i, Fig. 7), intensity does not decay after ~230 s of electron irradiation. In fact, the relative intensity increases from 0.26 to 0.41 during this time frame inferring greater retention of relative to oxygen losses. This also supports the 300 kV experiments at cryogenic
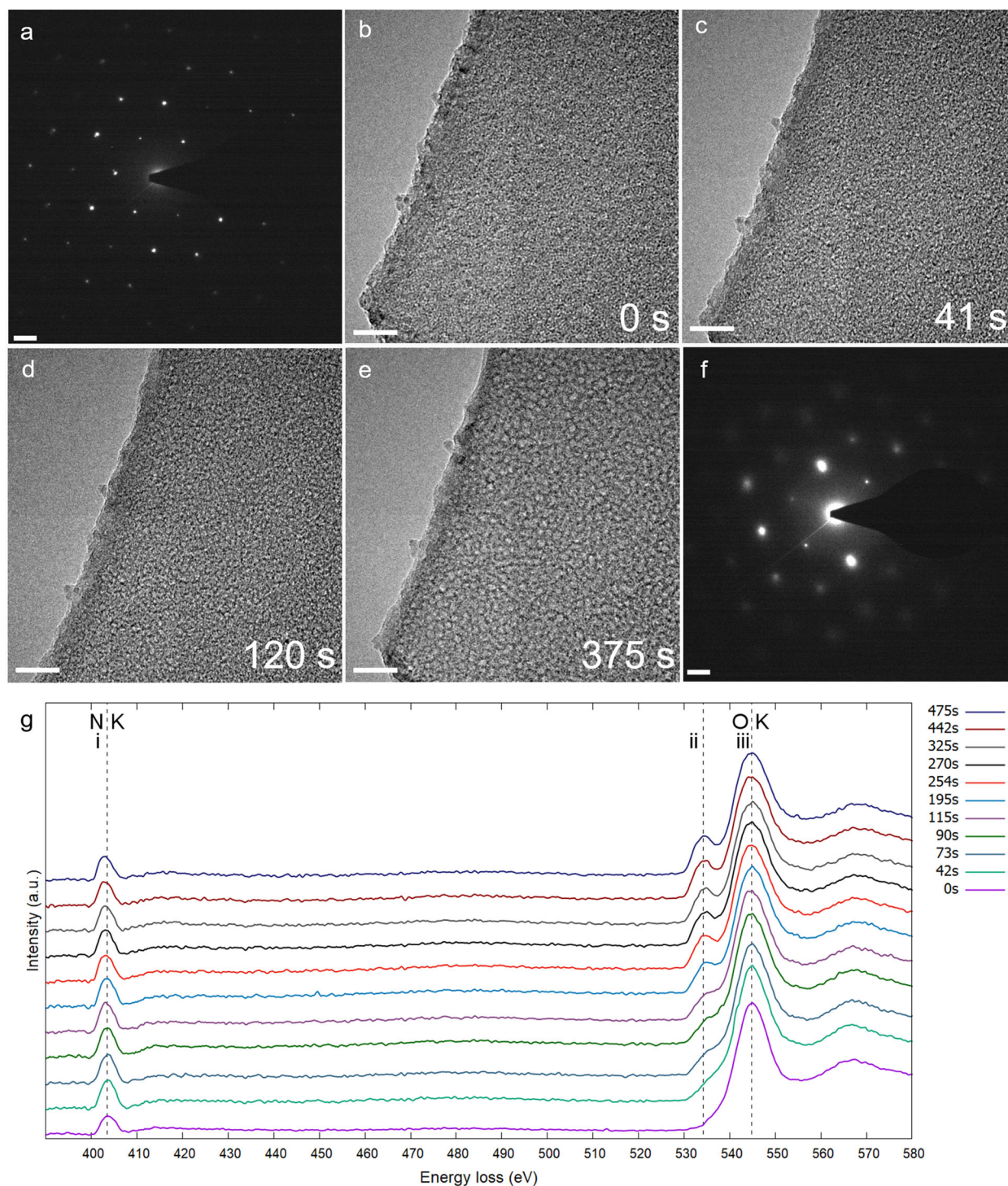
Fig. 5 Electron irradiation of Ni–Fe LDH at 300 kV at cryogenic temperatures. a, f Depict electron diffraction patterns of Ni–Fe LDH before and after irradiation experiments. **b–e** BFTEM series images during 300 kV irradiation when the sample is cooled to −180 °C in situ. Time-series core loss EELS spectra of the nitrogen K edge and oxygen K edge acquired from 0 to 475 s in (**g**). The time associated with the individual spectra indicates the electron irradiation time of the Ni–Fe LDH sample. Scale bars are 2 nm^{-1} for the SAED patterns and 20 nm for the BFTEM micrographs respectively.

temperatures (Fig. 5g) and further insinuates that the associated nitrogen-related mass-losses could be due to a heating effect as opposed to 'knock-on' or radiolytic mechanisms. In addition, the pre-peak intensity of the oxygen K edge (peak ii at 534 eV, Fig. 7) increases from 0 to 0.28 after 229 s and also attains a more prominent spectral shape. This perhaps relates to excessive dehydration of the LDH and generation of TMOs in comparison to

previous room temperature studies. Overall, the observed experimental phenomena may be explained by the following potential degradation pathways. Firstly, the electron beam displaces the hydrogen through 'knock-on' interactions by transferring energy directly to the atomic nucleus[20]. In addition, the sputtering of hydrogen may lead to augmented creations of secondary electrons and free radicals which can further
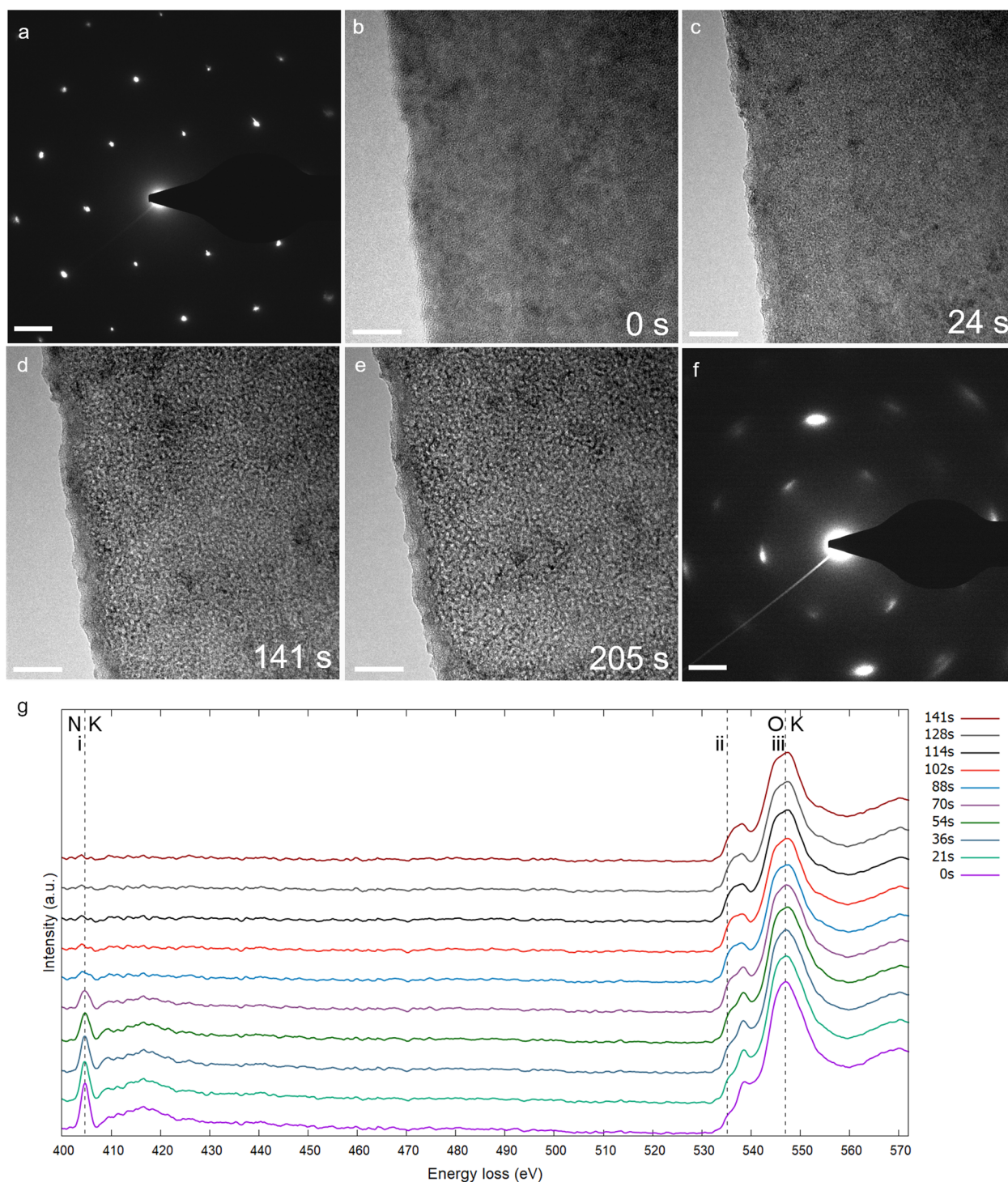
Fig. 6 Electron irradiation of Ni–Fe LDH at 80 kV. a SAED patterns of the Ni–Fe LDH before irradiation experiments. **b–e** Time series TEM images recorded after 0 s, 24 s, 141 s and 205 s of electron irradiation respectively. **f** Electron diffraction patterns of the irradiated region. **g** EELS spectra time series of the nitrogen and oxygen K edges recorded from the same LDH platelet from 0 to 141 s. Scale bars are 2 nm^{-1} for the SAED patterns and 20 nm for the BFTEM micrographs respectively.

contribute to radiolytic interactions. Simultaneously, hydrogen may also be removed through direct ionization of the OH$^-$ groups within the LDH cationic layers. This continued oxygen and hydrogen depletion leads to the removal and formation of unpaired oxygen. We propose that the exposed structures consequentially re-arrange to form TMO with the Ni or Fe sites, observed in the oxygen K edge evolution at both 300 and 80 kV EELS experiments. The latter voltage showcased an increased rate

of TMO generation, perhaps indicating that the radiolytic dehydroxylation mechanism is more prevalent[40]. Subsequently, the dehydroxylation diminishes the interlayer electrostatic interactions with the anionic species such as NO$_3^-$ and H$_2$O. This, in turn, facilitates the escape of nitrogen-related anions through interlayer gallery spaces or generated pores. For this stage of the degradation process, we further propose that this mass-loss is governed by diffusion or vibrational means during structural
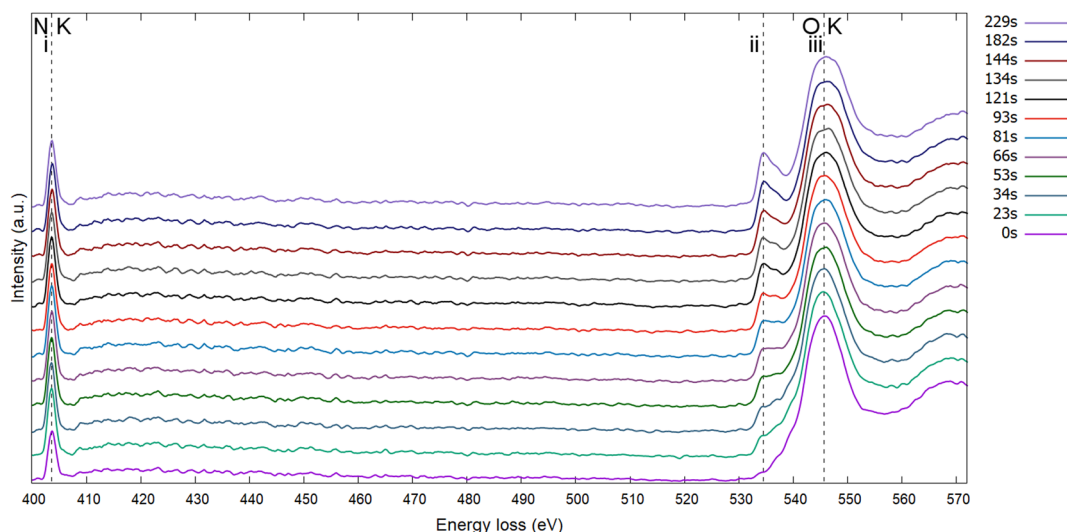
Fig. 7   Ni–Fe LDH core loss EELS time series of the nitrogen and oxygen K edge analysed at 80 kV while the sample is cooled to −180 °C. The time of the EEL spectra accounts for the total irradiation time of the sampled region at acquisition from 0 to 229 s.

re-arrangement of the H-deprived structures. Similar mechanisms have also been addressed from the thermal degradations of LDH materials[41]. This mass-loss can be depicted by nitrogen peak intensity attenuation only during room temperature irradiation experiments. The unperturbed nitrogen peak intensity during EELS experiments at cryogenic temperatures (Figs 5g and 7) suggests there is an immobilization of the liberated nitrates preventing the associated anionic mass-losses from the interlayer galleries.In this report, we demonstrated that electron beam interactions in the TEM can significantly affect the physical and chemical features of Ni–Fe layered double hydroxides. During irradiation of the specimen, the structural integrity was compromised. Porous voids were found to develop within the hexagonal nanoplatelets which were accompanied by a disordering of the LDH hexagonal crystal structure towards an amorphous phase. The electronic structure of the Ni–Fe LDH was also observed to change upon electron irradiation. Core loss EELS time-series studies of the nitrogen and oxygen K edges indicated a dehydroxylation of the cationic layers to TMO species followed by mass losses due to the escape of interlayer anions. These transformation behaviours were profoundly affected by the TEM imaging conditions. Ni–Fe LDHs were found to be less susceptible to structural changes during electron irradiation at 300 kV, where atomic displacement damage mechanisms dominate. However, radiolytic effects cannot be ruled out of the transformation process. Cooling the NiFe LDH specimen in situ had no major effect on the dehydroxylation of the LDH material, evidenced by the formation of the oxygen K edge pre-peak at both column and cryogenic temperatures. This cooling did however mitigate the escape of nitride structures within the material, showcasing that the anionic mass-losses are caused by thermal effects such as diffusion rather than atomic displacement or radiolysis by incoming electrons. The rate of LDH hydrogen removal, depicted by oxygen pre-peak generation, increased when the incident electron energy was reduced from 300 to 80 kV. Hence, we suggest that the LDH material is more susceptible to radiolytic rather than 'knock-on' effects. These findings give a deeper insight into the decomposition pathways of Ni–Fe LDHs during observed electron irradiation phenomena. Moreover, the role of characterization conditions may provide vital information into the next stage of understanding and interpretation of fundamental properties of all types of layered double hydroxide nanomaterials.

METHODS

TEM sample preparation

The LDH samples were synthesized as described in previous work conducted by our research group[23]. Samples were prepared for TEM by placing 3 µl of the sample dispersion on a lacey carbon film copper TEM grid (Ted Pella, USA). The excess sample was wicked away and the sample was baked overnight before each TEM experiment.

TEM and EELS characterisation

The LDH materials were analysed in an FEI Titan TEM (Thermo Fisher Scientific, OR, USA) at both 80 and 300 kV. EELS experiments were conducted using an equipped Gatan Imaging Filter (Gatan Inc., CA, USA). Typically, EEL spectra were acquired with a dispersion of 0.1 eV/channel with an energy resolution of ~1 eV (FWHM of the zero-loss peak) and an entrance aperture of 2 mm on the spectrometer. Samples were cooled to liquid nitrogen temperatures in situ using a cryogenic TEM sample holder (Fischione Instruments, PA, USA). Aberration-corrected scanning TEM was also used to characterize the Ni–Fe LDH nanomaterials using a NION UltraSTEM (NION, WA, USA). The electron dose rate was kept consistent throughout the TEM analyses of this study by maintaining a constant illumination area of the sample and beam current as read out by the phosphor screen of the TEM. For each imaging condition, a fresh unimaged area was used when recording images and EEL spectra.

DATA AVAILABILITY

The related data presented in the findings of this work is available from the corresponding author upon reasonable request.

REFERENCES

1. Manna, N., Ayasha, N., Singh, S. K. & Kurungot, S. A NiFe layered double hydroxide-decorated N-doped entangled-graphene framework: a robust water oxidation electrocatalyst. *Nanoscale Adv.* **2**, 1709–1717 (2020).
2. Wang, F. et al. One-step synthesis of Nickle Iron-layered double hydroxide/reduced graphene oxide/carbon nanofibres composite as electrode materials for asymmetric supercapacitor. *Sci. Rep.* **8**, 1–10 (2018).
3. Monjoghtapeh, R. H., Zardkhoshoui, A. M. & Hosseiny Davarani, S. S. Hierarchical MnCo2S4 nanowires/NiFeLDH nanosheets/graphene: a promising binder-free positive electrode for high-performance supercapacitors. *Electrochim. Acta* **338**, 135891 (2020).

4. Gong, M. et al. An advanced Ni-Fe layered double hydroxide electrocatalyst for water oxidation. *J. Am. Chem. Soc.* **135**, 8452–8455 (2013).

5. Wang, D. et al. Atomic and electronic modulation of self-supported nickel-vanadium layered double hydroxide to accelerate water splitting kinetics. *Nat. Commun.* **10**, 1–12 (2019).

6. Costard, L. S. et al. Layered double hydroxide as a potent non-viral vector for nucleic acid delivery using gene-activated scaffolds for tissue regeneration applications. *Pharmaceutics* **12**, 1219 (2020).

7. Jiang, X. X. et al. Ultrathin sulfate-intercalated NiFe-layered double hydroxide nanosheets for efficient electrocatalytic oxygen evolution. *RSC Adv.* **10**, 12145–12150 (2020).

8. Zhang, X. et al. A simple synthetic strategy toward defect-rich porous monolayer NiFe-layered double hydroxide nanosheets for efficient electrocatalytic water oxidation. *Adv. Energy Mater.* **9**, 1–7 (2019).

9. Fan, G., Li, F., Evans, D. G. & Duan, X. Catalytic applications of layered double hydroxides: recent advances and perspectives. *Chem. Soc. Rev.* **43**, 7040–7066 (2014).

10. Wang, Q. & Hare, D. O. Recent advances in the synthesis and application of layered double hydroxide (LDH) nanosheets. *ACS Chem. Rev.* **112**, 4124–4155 (2012).

11. Zhao, Y. et al. Sub-3 nm Ultrafine Monolayer Layered Double Hydroxide Nanosheets for Electrochemical Water Oxidation. *Adv. Energy Mater.* **8**, 1–8 (2018).

12. Zhang, J. et al. Single-atom Au/NiFe layered double hydroxide electrocatalyst: probing the origin of activity for oxygen evolution reaction. *J. Am. Chem. Soc.* **140**, 3876–3879 (2018).

13. Wang, Z. et al. Single Ru atoms with precise coordination on a monolayer layered double hydroxide for efficient electrooxidation catalysis. *Chem. Sci.* **10**, 378–384 (2019).

14. Jose, N. A., Zeng, H. C. & Lapkin, A. A. Hydrodynamic assembly of two-dimensional layered double hydroxide nanostructures. *Nat. Commun.* **9**, 1–12 (2018).

15. Muller, D. A. Structure and bonding at the atomic scale by scanning transmission electron microscopy. *Nat. Mater.* **8**, 263–270 (2009).

16. Jiang, N. Electron beam damage in oxides: a review. *Rep. Prog. Phys.* 79, (2015).

17. Egerton, R. F. Radiation damage to organic and inorganic specimens in the TEM. *Micron* **119**, 72–87 (2019).

18. Chen, Q. et al. Imaging beam-sensitive materials by electron microscopy. *Adv. Mater.* **32**, 1–42 (2020).

19. Freeman, H. M., Perez, J. P. H., Hondow, N., Benning, L. G. & Brown, A. P. Beam-induced oxidation of mixed-valent Fe (oxyhydr)oxides (green rust) monitored by STEM-EELS. *Micron* **122**, 46–52 (2019).

20. Su, D., Jiang, N., Spence, J. C. H., He, F. & Petuskey, W. T. On the dehydration mechanism of Mg (OH) 2 by a high-energy electron beam. *J. Appl. Phys.* **104**, 1–5 (2008).

21. Gomez-Villalba, L. S., Sierra-Fernandez, A., Milosevic, O., Fort, R & Rabanal, M. E. Atomic scale study of the dehydration/structural transformation in micro and nanostructured brucite (Mg(OH)2) particles: influence of the hydrothermal synthesis conditions. *Adv. Powder Technol.* **28**, 61–72 (2017).

22. Abellán, G. et al. Stimuli-responsive hybrid materials: breathing in magnetic layered double hydroxides induced by a thermoresponsive molecule. *Chem. Sci.* **6**, 1949–1958 (2015).

23. Jaskaniec, S. et al. Low-temperature synthesis of high quality Ni-Fe layered double hydroxides hexagonal platelets. *Sci. Rep.* **8**, 4–11 (2018).

24. Hobbs, C. et al. Structural transformation of layered double hydroxides: an in situ TEM analysis. *npj 2D Mater. Appl.* **2**, 4 (2018).

25. Ahn, C. C. & Krivanek, O. EELS Atlas: a reference collection of electron energy loss spectra covering all stable elements. (Warrendale, Gatan, 1983).

26. Colliex, C., Manoubi, T. & Ortiz, C. Electron-energy-loss-spectroscopy near-edge fine structures in the iron-oxygen system. *Phys. Rev. B* **44**, 11402–11411 (1991).

27. Leapman, R. D., Grunes, L. A. & Fejes, P. L. Study of the L23 edges in the 3d transition metals and their oxides by electron-energy-loss spectroscopy with comparisons to theory. *Phys. Rev. B* **26**, 614–635 (1982).

28. van Aken, P. A. & Langenhorst, F. Nanocrystalline, porous periclase aggregates as product of brucite dehydration. *Eur. J. Mineral.* **13**, 329–341 (2001).

29. Gomez-Villalba, L. S., Sierra-Fernandez, A., Rabanal, M. E. & Fort, R. TEM-HRTEM study on the dehydration process of nanostructured Mg-Ca hydroxide into Mg-Ca oxide. *Ceram. Int.* **42**, 9455–9466 (2016).

30. Grunes, L. A., Leapman, R. D., Wilker, C. N., Hoffmann, R. & Kunz, A. B. Oxygen K near-edge fine structure: an electron-energy-loss investigation with comparisons to new theory for selected 3d transition-metal oxides. *Phys. Rev. B* **25**, 7157–7173 (1982).

31. Gázquez, J. et al. Applications of STEM-EELS to complex oxides. *Mater. Sci. Semicond. Process.* **65**, 49–63 (2017).

32. Jiang, N. Structure and composition dependence of oxygen K edge in CaAl$_2$O$_4$. *J. Appl. Phys.* **100**, 013703 (2006).

33. Van Aken, P. A., Liebscher, B. & Styrsa, V. J. Core level electron energy-loss spectra of minerals: pre-edge fine structures at the oxygen K-edge. *Phys. Chem. Miner.* **25**, 494–498 (1998).

34. Tan, H., Verbeeck, J., Abakumov, A. & Tendeloo, G. Van. Oxidation state and chemical shift investigation in transition metal oxides by EELS. *Ultramicroscopy* **116**, 24–33 (2012).

35. Kurata, H., Lefèvre, E., Colliex, C. & Brydson, R. Electron-energy-loss near-edge structures in the oxygen K-edge spectra of transition-metal oxides. *Phys. Rev. B* **47**, 13763–13768 (1993).

36. Mitterbauer, C. et al. Electron energy-loss near-edge structures of 3d transition metal oxides recorded at high-energy resolution. *Ultramicroscopy* **96**, 469–480 (2003).

37. Gilks, D. et al. Atomic and electronic structure of twin growth defects in magnetite. *Sci. Rep.* **6**, 1–8 (2016).

38. Hwang, S. et al. Using real-time electron microscopy to explore the effects of transition-metal composition on the local thermal stability in charged LixNiyMnzCo1-y-zO2 cathode materials. *Chem. Mater.* **27**, 3927–3935 (2015).

39. Zhang, D. et al. Atomic-resolution transmission electron microscopy of electron beam–sensitive crystalline materials. *Science* **359**, 675–679 (2018).

40. Mkhoyan, K. A., Silcox, J., McGuire, M. & Disalvo, F. J. Radiolytic purification of CaO by electron beams. *Philos. Mag.* **86**, 2907–2917 (2006).

41. Yu, G. et al. Dehydration and dehydroxylation of layered double hydroxides: new insights from solid-state NMR and FT-IR studies of deuterated samples. *J. Phys. Chem. C* **119**, 12325–12334 (2015).

ACKNOWLEDGEMENTS

AUTHOR CONTRIBUTIONS

C.H. and V.N. designed the study. S.J. synthesized the materials characterized throughout this work. C.H. prepared TEM samples and conducted TEM, electron diffraction and EELS experiments and analyses. C.D. performed aberration-corrected HAADF-STEM experiments. C.H. and C.D. interpreted experimental results. C.H. and V.N. wrote the paper with contributions from all authors.

COMPETING INTERESTS

The authors declare no competing interests.

ADDITIONAL INFORMATION